

Dispersion engineering in spin-orbit coupled spinor $F = 1$ condensates driven by negative masses

K. Rajaswathi,¹ S. Bhuvanewari,² R. Radha,² and P. Muruganandam¹

¹*Department of Physics, Bharathidasan University, Tiruchirappalli 620024, Tamil Nadu, India*

²*Centre for Nonlinear Science (CeNSc), Government College for Women, Kumbakonam 612001, Tamil Nadu, India*

(Dated: April 19, 2023)

We investigate the impact of negative mass on expanding spin-orbit (SO) coupled spinor $F = 1$ Bose-Einstein condensates by analyzing the dispersion relation of the single-particle quantum system. In SO-coupled spinor condensates, a negative mass parameter generates a wave packet that propagates in the opposite direction of the momentum. We analyze the dynamics of spin waves analytically and present a simple approach to investigate the expansion of spinor condensates. In particular, we examine the dynamics when both masses are negative, which results in the spinor condensate splitting into two counter-propagating self-interfering packets (SIPs). Using numerical simulations of the coupled Gross-Pitaevskii equations, we demonstrate the density expansion and self-interference patterns with and without magnetization for repulsive and attractive interactions with different coupling parameters. Our investigation has unearthed several phenomena observed in experiments, such as symmetric expansion dynamics, SIPs, pileup, modulation instability, slow down, and self-trapping. Furthermore, we notice that a phase diagram of expansion velocities could be used to identify a quantum phase transition, from a plane wave phase to a stripe phase, based on the strengths of SO coupling, Rabi coupling, and interaction.

I. INTRODUCTION

The interaction between a quantum particle's spin and momentum, known as spin-orbit coupling (SOC), has opened up numerous avenues in quantum science [1, 2]. This peculiar yet fascinating field of research finds applications in almost all branches of physics like for example, topological insulators [3, 4], spin Hall effect [5], Majorana fermions [6], spintronic devices [7], and quantum computing applications [8]. Recently, Bose-Einstein condensation (BEC), which belongs to the class of ultracold atoms, has provided an excellent platform for conducting quantum studies beyond natural conditions. One of the major challenges in this investigation is that the atoms are neutral, and coupling with the gauge field requires engineering synthetic gauge fields. To overcome this inherent issue of neutrality, several proposals have been put forward to realize synthetic gauge fields for quantum gases [9–12].

In the past few years, research on synthetic gauge fields has evolved towards the “*on-demand*” engineering of spin-orbit coupling (SOC) using laser beams. This field of research is promising due to its ability to realize exotic configurations of nontrivial topology and simulate vital electronic phenomena in condensed matter physics. The Spielman group at NIST made a seminal contribution to this exciting field by engineering the SOC in neutral Bose-Einstein condensates (BECs) using a pair of lasers to dress two atomic spin states [2, 13]. They achieved momentum-sensitive coupling in ^{87}Rb , which has equal contributions from Rashba and Dresselhaus, by using a pair of Raman lasers to address two of its $F = 1$ hyperfine spin states: $|\uparrow\rangle = |F = 1, m_F = 0\rangle$ and $|\downarrow\rangle = |F = 1, m_F = -1\rangle$.

Following the pioneering work of the Spielman group at NIST [13], synthetic SOC has been successfully engi-

neered with both neutral bosonic and fermionic ultracold atoms [14], which not only exhibits many exotic phases, but also opens up a lot of avenues to explore novel SOC physics with an unprecedented level of tunability of experimental parameters. Taking advantage of the exceptional tunability of experimental parameters, SOC in BEC presents an exciting possibility of engineering more complex dispersion relations through controlling the Raman laser setup. One of the fundamental studies in this direction is the concept of negative mass by suitably engineering the dispersion relation in diverse quantum systems. The negative mass is a hypothetical concept of matter whose mass is of opposite sign to the mass of normal matter, say, for example, -2kg . Such matter may violate some energy conditions and exhibit strange characteristics [15]. Recently, Khomechi *et al.* have shown how the peculiar dispersion relation of an atomic spin-orbit coupled Bose-Einstein condensate could lead to unconventional wave packet dynamics, interpreted as negative-mass hydrodynamics and reported phenomena such as self-trapping, soliton trains, and dynamical instabilities [16]. Zhao *et al.* [17] reported a study on the periodic transition between negative and positive inertial mass with AC oscillation of a spin soliton driven by a constant force. They further discussed the weak force that could be diagnosed from the AC oscillation phenomena of the spin soliton, which is similar to recent experiments observed in optomechanical instruments. Farolfi *et al.* investigate the collisional dynamics of magnetic solitons in a harmonically trapped binary mixture using phase imprinting [18]. Following their work, Chai *et al.* reported a magnetic soliton in a spin-1 Bose-Einstein condensate using the magnetic phase imprinting method and observed good agreement with numerical simulations based on the one-dimensional Gross-Pitaevskii equation [19]. Meng *et al.* investigated spin solitons employing the dispersion

relation with critical velocities to demarcate the boundary between negative and positive mass regimes. A correlation between the width and speed helped them to distinguish between bright and dark solitons [20].

A more comprehensive theoretical study on the negative mass effect in SO-coupled BECs was reported recently by Colas *et al.* [21]. In this work, the authors have discussed the conceptual evidence and the physical interpretation of the negative masses beyond the description reported in Ref. [16]. They have also brought out the characteristics of several regimes that determine the signs of different effective mass parameters, say m_1 and m_2 derived from energy-dispersion relation. At this juncture, it is worth pointing out that both these investigations on the negative mass effect were centered around SO-coupled spin-1/2 BECs, which means that the ramifications of negative mass on SOC spinor $F = 1$ BECs have still not yet been explored. Thus, inspired by the distinct features of SO coupling and the physical relevance of the $F = 1$ system, we intend to study the dynamic behavior of negative mass in SO-coupled BECs. In this paper, we investigate the impact of negative mass in spin-orbit coupled $F = 1$ spinor condensates. First, we discuss the situation at the single-particle level showing the peculiar features of the single-particle energy spectrum. We then study the dynamics in a regime where both the masses, m_1 and m_2 , are negative.

The paper is organized as follows: After a detailed introduction, Sec. II presents the theoretical model that describes the concept of negative mass and the Hamiltonian of the problem under investigation. The energy dispersion relation and the characteristics of the dispersion curve are discussed in Sec. III. In Sec. IV, we bring out through numerical simulation several interesting signatures of negative mass regimes like symmetric expansion, self-interference pattern (SIP), etc. We then conclude with the highlights of the investigation in Sec. V.

II. THEORETICAL MODEL

We review the fundamental concepts of negative mass using the energy dispersion relation [22]. Expanding the energy dispersion relation up to the second-order, we get $E(p) = E_0 + v_g(p - p_0) + (p - p_0)^2/[2m_2(p_0)]$, which can be used to deduce two mass parameters m_1 and m_2 that dictate the dynamics of the system under consideration by

$$m_1 = \frac{p}{v_g} = p \left(\frac{\partial E}{\partial p} \right)^{-1} \quad (1a)$$

$$m_2 = \left(\frac{\partial^2 E}{\partial p^2} \right)^{-1}. \quad (1b)$$

Both mass parameters are equally important if one has to consider both the propagation and diffusion of wave packets. In an isotropic system, the mass parameters m_1 and m_2 are respectively related to the group velocity and

the acceleration of wave packets as given by Eq. (1). In the case of anisotropic materials, the above relations hold with a slight modification such that the particle momentum and velocity can be related as $p_i = m_{ij}v_j$, where m_{ij} is the effective mass tensor, p_i and $v_j(i, j = x, y, z)$ are components of momentum and velocity, respectively. For the present study, we adopt the experimental realization of tunable SO-coupled BEC in ^{87}Rb reported by Lin *et al.* [13]. In that configuration, two counter-propagating Raman lasers of wavelength (λ_r) are used to couple the states with strength Ω . The Raman wave vector is given by $k_L = 2\pi \sin(\beta_r/2)/\lambda_r$, where β_r is the orientation of Raman lasers.

In this context, we consider the SO coupling among the three spin components of the $F = 1$ hyperfine state $5S_{1/2}$ of ^{87}Rb , namely, $|F = 1, m_F = 1\rangle$, $|F = 1, m_F = 0\rangle$ and $|F = 1, m_F = -1\rangle$, where m_F is the z projection of F [23]. Then, the single-particle Hamiltonian of the quasi-hyperfine spin-1 SO-coupled BEC confined along the x axis by a strong transverse trap along y and z axes can be written as

$$H_0 = \frac{p_x^2}{2m} + k_L p_x \Sigma_z + V(x) + \Omega \Sigma_x. \quad (2)$$

We consider three possible SO couplings in the above Hamiltonian of the form $k_L p_x \Sigma_x$, $k_L p_x \Sigma_y$ and $k_L p_x \Sigma_z$, where k_L is the SO coupling parameter, Ω is the Rabi frequency, $V(x)$ is the trapping potential, $p_x = -i\hbar\partial_x$ is momentum operator, Σ_x , Σ_y and Σ_z are the spinor-1 angular momentum operators which are given by

$$\Sigma_x = \frac{1}{\sqrt{2}} \begin{pmatrix} 0 & 1 & 0 \\ 1 & 0 & 1 \\ 0 & 1 & 0 \end{pmatrix}, \quad \Sigma_y = \frac{i}{\sqrt{2}} \begin{pmatrix} 0 & -1 & 0 \\ 1 & 0 & -1 \\ 0 & 1 & 0 \end{pmatrix},$$

$$\Sigma_z = \begin{pmatrix} 1 & 0 & 0 \\ 0 & 0 & 0 \\ 0 & 0 & -1 \end{pmatrix}. \quad (3)$$

In the standard computational basis, the matrix notation of the Hamiltonian is

$$H_0 = \begin{pmatrix} \frac{p_x^2}{2m} + p_x k_L & \frac{\Omega}{\sqrt{2}} & 0 \\ \frac{\Omega}{\sqrt{2}} & \frac{p_x^2}{2m} & \frac{\Omega}{\sqrt{2}} \\ 0 & \frac{\Omega}{\sqrt{2}} & \frac{p_x^2}{2m} - p_x k_L \end{pmatrix}. \quad (4)$$

By setting the trapping potential zero, energy eigenspectrum corresponding to the homogeneous non-interacting SO coupled BEC can be written as

$$\omega_{y,z}(p) = \frac{p_x^2}{2m} \quad \text{and} \quad \omega_{\pm y,z}(p) = \frac{p_x^2}{2m} \pm \sqrt{\Omega^2 + p_x^2 k_L^2}. \quad (5)$$

If we consider SO coupling along the y or z axis, the eigenvalues remain the same. On the other hand, the energy of the system considering SO coupling along x

axis is given by

$$\omega_x(p) = \frac{p_x^2}{2m} \text{ and } \omega_{\pm x}(p) = \frac{p_x^2}{2m} \pm k_L p_x - \Omega. \quad (6)$$

Under the Hartree approximation, the spinor BEC in a quasi-1D trap can be described by a set of three coupled Gross-Pitaevskii equations for the three components of wave function ψ_j , $j = -1, 0, +1$ as [24–28]

$$i\hbar \frac{\partial \Psi_{\pm 1}}{\partial t} = \left[-\frac{\hbar^2}{2m} \frac{\partial^2}{\partial x^2} + V(x) + c_0 n + c_2(n_{\pm 1} + n_0 - n_{\mp 1}) \right] \Psi_{\pm 1} + c_2 \Psi_0^2 \Psi_{\mp 1}^* + \frac{\Omega}{\sqrt{2}} \Psi_0 \mp i\hbar k_L \frac{\partial \Psi_{\pm 1}}{\partial x}, \quad (7a)$$

$$i\hbar \frac{\partial \Psi_0}{\partial t} = \left[-\frac{\hbar^2}{2m} \frac{\partial^2}{\partial x^2} + V(x) + c_0 n + c_2(n_{+1} + n_{-1}) \right] \Psi_0 + 2c_2 \psi_{+1} \Psi_{-1} \Psi_0^* + \frac{\Omega}{\sqrt{2}} (\Psi_{+1} + \Psi_{-1}), \quad (7b)$$

with

$$c_0 = \frac{2\hbar^2(a_0 + 2a_2)}{3ml_{yz}^2}, \quad c_2 = \frac{2\hbar^2(a_2 - a_0)}{3ml_{yz}^2}, \quad (8)$$

where a_0 and a_2 are the s -wave scattering lengths in the total spin 0 and 2 channels, respectively. $n = \sum_j n_j$ is the total density with $n_j = |\Psi_j|^2$, $j = 1, 0, -1$ are the densities of the individual spin components.

We choose spin-1 ^{87}Rb atoms with scattering lengths $a_0 = 101.8a_B$ and $a_2 = 100.4a_B$, where a_B is the Bohr radius and use the experimental trapping frequency range $2\pi \times 230$ Hz [29] in our numerical simulations. If $c_0 > 0$ and $c_2 < 0$, the interaction is repulsive, while it is attractive for $c_0 < 0$ and $c_2 < 0$ [28, 30] and the concept of Feshbach resonance can be employed for manipulating the scattering lengths [31, 32] to determine the characteristics of the condensates [33].

The harmonic trap is given as, $V(x) = m\omega_x^2 x^2/2$ and $l_{yz} = \sqrt{\hbar/(m\omega_{yz})}$ is the oscillator length in the transverse $y-z$ plane, where $\omega_{yz} = \sqrt{\omega_y \omega_z}$. The normalization condition is

$$\int_{-\infty}^{\infty} dx \sum_{j=-1}^1 |\Psi_j(x)|^2 = N. \quad (9)$$

In the above, N is the total number of atoms, which is of the order of 10^3 and $l_0 = \sqrt{\hbar/m\omega_x}$ is the oscillator length along the x -axis.

It is convenient to transform Eq. (7) into dimensionless form, for which we use the following change of variables,

$$x = l_0 \tilde{x}, \quad t = \omega_x^{-1} \tilde{t}, \quad \Psi(x, t) = N^{\frac{1}{2}} l_0^{-\frac{1}{2}} \psi_j(\tilde{x}, \tilde{t}). \quad (10)$$

By applying the change of variables (10) to (7), the cou-

pled GP equations can be expressed as,

$$i \frac{\partial \psi_{\pm 1}}{\partial t} = \left[-\frac{1}{2} \frac{\partial^2}{\partial \tilde{x}^2} + \tilde{V} + \tilde{c}_0 \tilde{n} + \tilde{c}_2(\tilde{n}_{\pm 1} + \tilde{n}_0 - \tilde{n}_{\mp 1}) \right] \psi_{\pm 1} + \tilde{c}_2 \psi_0^2 \psi_{\mp 1}^* + \frac{\tilde{\Omega}}{\sqrt{2}} \psi_0 \mp i\hbar \tilde{k}_L \frac{\partial \psi_{\pm 1}}{\partial x}, \quad (11a)$$

$$i \frac{\partial \psi_0}{\partial t} = \left[-\frac{1}{2} \frac{\partial^2}{\partial \tilde{x}^2} + \tilde{V} + \tilde{c}_0 \tilde{n} + \tilde{c}_2(\tilde{n}_{+1} + \tilde{n}_{-1}) \right] \psi_0 + 2\tilde{c}_2 \psi_{+1} \psi_{-1} \psi_0^* + \frac{\tilde{\Omega}}{\sqrt{2}} (\psi_{+1} + \psi_{-1}), \quad (11b)$$

with

$$\tilde{c}_0 = \frac{2Nl_0(a_0 + 2a_2)}{3l_{yz}^2}, \quad \tilde{c}_2 = \frac{2Nl_0(a_2 - a_0)}{3l_{yz}^2}, \quad (12)$$

where $\tilde{V} = \tilde{x}^2/2$, $\tilde{k}_L = \hbar k_r/m\omega_x l_0$, $\tilde{\Omega} = \Omega/\hbar\omega_x$, $\tilde{n}_j = |\psi_j|^2$ with $j = 1, 0, -1$ and $\tilde{n} = \sum_{j=-1}^1 |\psi_j|^2$. Since the number of atoms N is absorbed in the dimensionless quantities, the normalization and magnetization conditions satisfied by the ψ_j 's become

$$\int_{-\infty}^{\infty} \sum_{j=-1}^1 \tilde{n}_j(\tilde{x}) d\tilde{x} = 1, \quad (13)$$

and

$$M = \int_{-\infty}^{\infty} [\tilde{n}_1(\tilde{x}) - \tilde{n}_{-1}(\tilde{x})] d\tilde{x} \quad (14)$$

For the sake of simplicity of notation, we denote the dimensionless variables without a tilde in the rest of the paper. The numerical results are discussed in Sec. IV for repulsive and attractive interactions with and without magnetization.

III. ANALYTICAL RESULTS

The energy dispersion relation is the fundamental framework of the investigation which governs the dynamics of the underlying dynamical system. It is evident from Eq. (5) that the energy spectrum consists of two branches. The \pm sign denotes the different helicity basis corresponding to either parallel or anti-parallel spin-index with reference to the wave vector. It is interesting to note that in the conventional BECs, the atoms condense at the ground state often recognized as a non-degenerate zero-momentum state, which does not occur in the SO-coupled BECs where one comes across multiple lowest degenerate energy states due to nonparabolic energy-momentum dispersion, unlike the conventional BECs. Figs. 1(a) and 1(b) show the energy spectrum corresponding to BEC without and with SO-coupling and Rabi coupling respectively. It is quite obvious from the above that the energy spectrum exhibits a single free-particle parabolic dispersion demonstrating the lowest

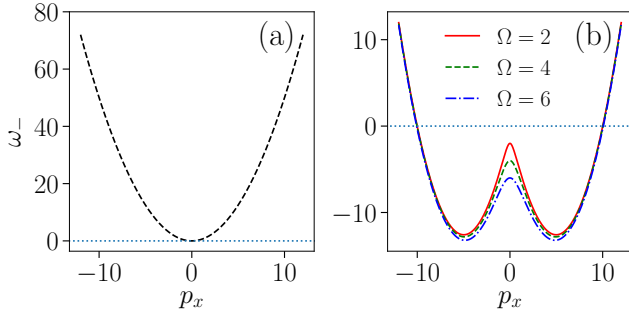


FIG. 1. Plots of (a) energy dispersion in the absence of spin-orbit coupling and (b) energy dispersion as a function of momentum for representative values of Rabi coupling with fixed parameters of $m = 1$ and $k_L = 5$.

energy state in the absence of the spin-orbit and Rabi couplings, i.e. $\omega_{\pm} = p_x^2/2m$. In other words, without SO coupling, the Hamiltonian represented by Eq. (4) has a unique minimum at $p_x = 0$ as shown in Fig. 1(a). It is straightforward to note from the expressions of the mass parameters that purely parabolic dispersion amounts to equal values of m_1 and m_2 . As evident from Fig. 1(b), the SO coupling changes the energy spectrum considerably leading to a non-parabolic energy dispersion, where the two mass parameters cannot be equal. In the present case, we identify the non-parabolic energy dispersion as a consequence of the negative effective mass parameter which is related to the negative curvature of the dispersion relation. Another notable feature is that the introduction of Rabi coupling when reinforced with the SO coupling generates a symmetric double-well potential as shown in Fig. 1(b) unlike the results reported in [21]. Dispersion with negative curvature plays an increasingly important role in quantum hydrodynamics, fluid dynamics, and optics. Manifestations of negative mass effects are observed in several quantum systems and the SOC-BECs can be exploited to witness controllable dispersion engineering through negative masses.

From the general expression given by Eq. (1), one can compute the mass parameters corresponding to the underlying system as

$$m_1 = \frac{m}{\left(1 - \frac{mk_L^2}{\sqrt{\Omega^2 + p_x^2 k_L^2}}\right)}, \quad (15a)$$

$$m_2 = \frac{m}{\left(1 - \frac{k_L^2 \Omega^2 m \sqrt{\Omega^2 + p_x^2 k_L^2}}{(\Omega^2 + p_x^2 k_L^2)^2}\right)}. \quad (15b)$$

As the dispersion regime and other related characteristics critically depend on the strength of the Rabi coupling, we show, in Figs. 2(a) and 2(b), the effective mass parameters in the momentum space for some representative values of Rabi coupling. It is evident from Fig. 2 that the effective mass is sensitive to the Rabi strength. As the strength of Rabi coupling increases, the negative region of both mass parameters shrinks, with m_2 being the most

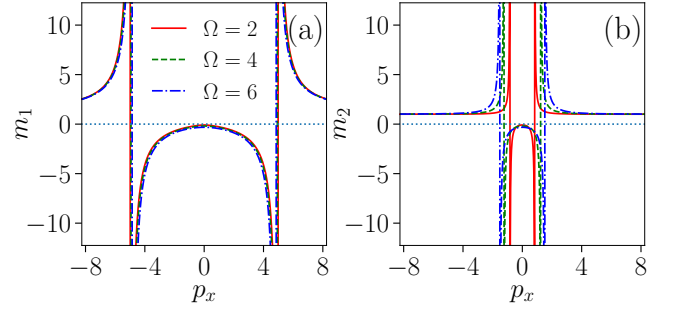


FIG. 2. Plots of (a) the variation of mass parameter m_1 and (b) the variation of mass parameter m_2 as a function of momentum are shown for a selected set of Rabi coupling strengths with fixed parameters $m = 1$ and $k_L = 5$.

sensitive to Ω than m_1 . The variation of the group velocity as a function of the momentum is portrayed in Fig. 3 using Eq. (1). The absolute value of the group velocity of the wave packet is found to be

$$v_- = \frac{p}{m} - \frac{pk_L^2}{\sqrt{\Omega^2 + p^2 k_L^2}}. \quad (16)$$

It is apparent from the above discussion that the mass parameters and the group velocity of the wave packets depend on the strength of the SO and Rabi couplings which is indeed a manifestation of the potential of the SO-coupled BECs for more effective dispersion engineering on quantum systems. In Fig. 4, we display the vari-

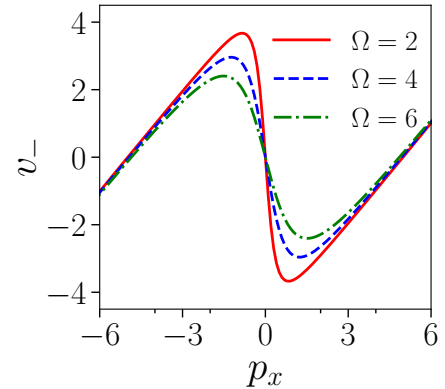


FIG. 3. Plot of group velocity as a function of p_x with fixed spin-orbit coupling ($k_L = 5$) and mass ($m = 1$) for different Rabi coupling strengths (Ω).

ation of the system parameters in the momentum space for some representative values of k_L and Ω corresponding to the lower branch of the energy spectrum. The inflection point representing the change of the sign of m_2 can be estimated using Eq. (1b) as ,

$$p_{x1,2} = \pm \sqrt{\left(\frac{m\Omega^2}{k_L}\right)^{2/3} - \left(\frac{\Omega}{k_L}\right)^2}. \quad (17)$$

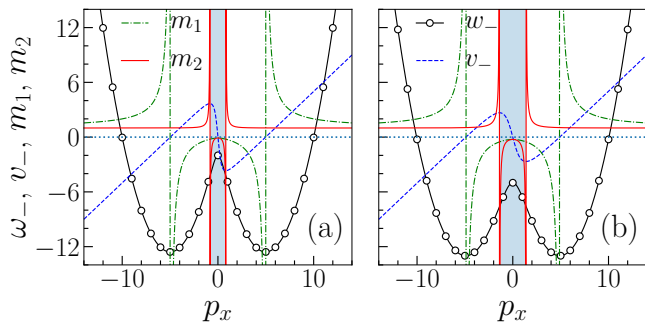


FIG. 4. Plots showing the variation of energy (solid black line with circles), group velocity (dashed blue line), and mass parameters (m_1 – dash-dotted green line and m_2 – solid red line) in momentum space presented for two different scenarios: (a) $k_L = 6$ and $\Omega = 2$, and (b) $k_L = 5$ and $\Omega = 5$, with a fixed parameter of $m = 1$.

Similarly, the points on the momentum space at which the effective mass m_1 diverges can be deduced from Eq. (1a) as follows

$$p_{x3,4} = \pm \sqrt{\frac{-\Omega^2 + m^2 k_L^4}{k_L}}. \quad (18)$$

In the parametric space of interest, one of the notable characteristic differences between the spin-1/2 reported in Ref. [21] and the present case of $F = 1$ is the shape of the energy spectrum. The energy dispersion spectrum is symmetric in the momentum space, as is evident from Fig. 4. It should be emphasized that the shape of the energy spectrum dictates the dynamics of the system under investigation. One can understand from Fig. 4 drawn out for two different sets of parameters that the energy spectrum, group velocity, and mass parameters depend on the strengths of Rabi coupling and SOC which means the shape of the energy spectrum can be manipulated accordingly leading to dispersion engineering.

It is worth observing from the above that one can interpret most of the dynamical behaviors of the system from the momentum-dependent velocity $v(p_x)$ given by Eq. (16), which can be straightforwardly related to the mass parameters m_1 and m_2 as defined by the expression (1). Fig. 4 shows how the group velocity, energy, and mass parameters vary in momentum space as a function of Rabi coupling and SOC. It can be observed from Figs. 4(a) and 4(b) that the linear part on either side of the zero momentum when the mass parameter m_2 diverges corresponds to a local maximum or minimum in the group velocity. The maximum and minimum are sensitive to the strength of the Rabi coupling as predicted earlier from Fig. 3. In addition, the point where the velocity becomes zero corresponds to the maxima of the energy dispersion curve, and the region where the velocity attains negative values corresponds to the domain where the energy dispersion curve tends to its minima. One of the key features of the velocity curve is the existence of the negative region owing to the negative mass

parameters where the wavepacket moves in the opposite direction in response to the impulse.

IV. NUMERICAL SIMULATIONS

We begin our simulation with an expanding spin-orbit coupled three-component spinor condensate with the time integration of the equation using the split-step method [34, 35]. The negative mass regime which has been associated with several interesting phenomena like self-interference pattern (SIP), self-trapping, etc., had earlier been observed by David Colas et al. for spin-1/2 spin-orbit coupled Bose-Einstein condensates by initially positioning the condensate at the bottom of the lower branch and releasing the trap from one side which is given by single band Gross-Pitaevskii equation [16, 21].

We adopt the same approach for spin-orbit coupled spinor $F = 1$ condensates and observe some of the dynamical phenomena like soliton train, dynamical instability, pileup, self-interference pattern (SIP) and self-trapping effects when the condensate starts to expand in the three different component densities ($|\psi_{+1}|^2$, $|\psi_0|^2$ and $|\psi_{-1}|^2$). To start with, we prepare the ground state wavefunctions of 1D harmonically trapped condensate by taking the initial condition as a Gaussian wave employing the imaginary-time propagation of the Gross-Pitaevskii equation (7). We study the dynamics by initially positioning the condensate at the bottom of the lower branch and releasing it from the harmonic trap during real-time propagation [36].

A. Expansion dynamics and self-interference

In a recent development, Su et al. demonstrated the self-interfering dynamics of a wave packet using the Wigner distribution function [37]. They observed the self-interfering dynamics in a non-interacting condensate by engineering dispersion using either optical lattice or spin-orbit coupling. Additionally, they observed asymmetric expansion dynamics by positioning the wave packet at the center ($x = 0$) and switching the initial quasimomentum between negative and positive values.

For the present investigation, the initial quasimomentum is taken as zero, which gives symmetric expansion. Here, density fluctuations are observed from the center to the tail of the condensate. This accumulation of density fluctuations, often referred to as “dynamical instability” at the edges, is called “pileup” and it occurs for different Rabi coupling strengths. The density fluctuations are much more pronounced when we increase Ω from 2 to 6 while keeping $k_L = 5$.

Moreover, the expansion of the condensate depends on the strength of the nonlinearities. For smaller nonlinearities, the wave packets expand faster and continuously. However, for larger nonlinearities, by increasing the number of atoms, the expansion slows down, and the conden-

sate stops expanding and becomes self-trapped, similar to the case of Bose-Einstein condensates in optical lattices by Wang et al., who studied larger nonlinearities with different atom numbers [38].

We first study self-interference packet (SIP) for the repulsive condensates with nonlinearities $c_0 = 0.25$ and $c_2 = -0.001$. Fig. 5 shows the condensate expansion for different values of Ω while keeping $k_L = 5$ and magnetization at zero.

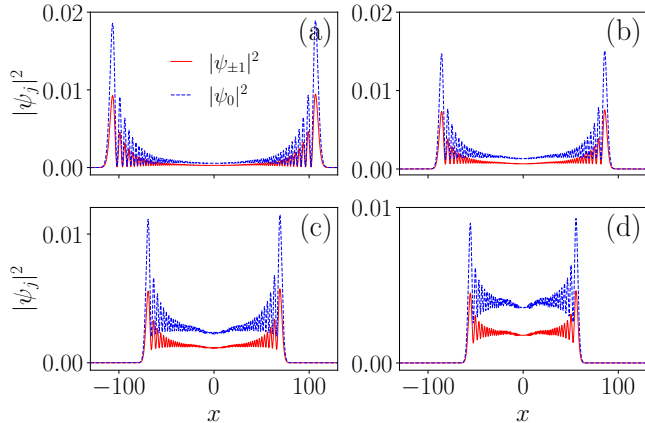


FIG. 5. The snapshots of the one-dimensional symmetric expansion of a spin-orbit coupled Bose-Einstein condensate without magnetization ($M = 0$) for $k_L = 5$ and for different values of (a) $\Omega = 2$, (b) $\Omega = 4$, (c) $\Omega = 6$, and (d) $\Omega = 8$ at $t = 30$.

We observe a symmetric expansion where the densities of $|\psi_{+1}|^2$ and $|\psi_{-1}|^2$ are equal, while $|\psi_0|^2$ has a different density. The snapshots at $t = 30$ are depicted in Figs. 5(a)-(d). Fig.5(a) shows fluctuations only at the edges when $\Omega = 2$. In contrast, Fig. 5(b) exhibits a decrease in density while the fluctuations begin to appear at the center to the edges, and the expansion slows down compared to Fig.5(a). The density is much smaller for $\Omega = 6$ and $\Omega = 8$, as shown in Figs. 5(c) and 5(d), respectively, and the fluctuations are observed from the center to the edges. Here, the expansion is slower compared to the other cases. The slower expansion rate of the condensate leads to an increase in the effective mass which is identical to that of Ref. [36]

Similarly, Fig. 6 shows the condensate expansion for different values of Ω , with $k_L = 5$ and a fixed magnetization of $M = 0.4$. All these figures are similar to Fig. 5, except that three distinct densities are observed for each case due to the removal of degeneracy, while the other observations remain the same as before.

Using real-time propagation, we perform a numerical simulation of the expansion of a quasi-1D ferromagnetic Bose-Einstein condensate (BEC) by releasing it from a harmonic trap. The densities of the spin components, $|\psi_j|^2$ ($j = 0, \pm 1$), at three different time instances are depicted in Figs. 7(a) - 7(c). Figs. 7(d) - 7(f) present a space-time plot of the densities, showing that the self-interaction causes the momentum distribution to

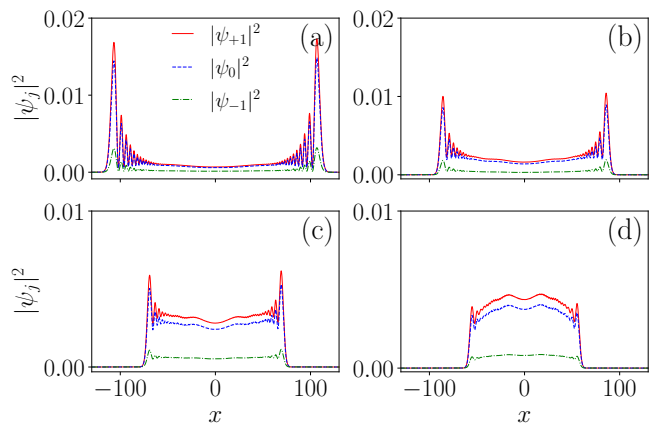


FIG. 6. The snapshots of the one-dimensional symmetric expansion of a spin-orbit coupled Bose-Einstein condensate with magnetization ($M = 0.4$) for $k_L = 5$ and for different values of (a) $\Omega = 2$, (b) $\Omega = 4$, (c) $\Omega = 6$, (d) $\Omega = 8$ at $t = 30$.

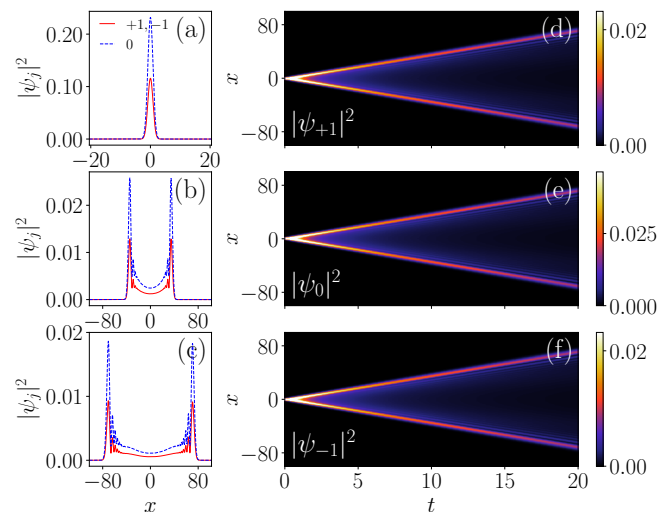


FIG. 7. Plots showing the expansion dynamics with coupling parameters $\Omega = 2$ and $k_L = 5$, numerically calculated with nonlinearities $c_0 = 0.25$ and $c_2 = -0.001$, for the case without magnetization. The 1D density plot at times $t = 0, 25$, and 50 is shown in panels (a), (b), and (c), respectively. Panels (d), (e), and (f) shows the dynamics of the spin component densities $|\psi_{+1}|^2$, $|\psi_0|^2$, and $|\psi_{-1}|^2$.

broaden, making them spread in real space. In the absence of magnetization, ψ_{+1} and ψ_{-1} have equal pseudo spin component densities. However, the presence of magnetic effects breaks the spin-1 component's degeneracy, leading to lower density fluctuations at the edges [29]. Figs. 7(d) and 7(f) exhibit the same density for ψ_{+1} and ψ_{-1} , whereas Fig. 7(e) shows a different density, ψ_0 , when the magnetization is zero.

Similarly, SIP is also observed in Figs. 8(a) to 8(c), which depict the component densities $|\psi_j|^2$ ($j = 0, \pm 1$) at three different instants of time. The space-time plot of the densities is shown in Figs. 8(d) to 8(f) when the

magnetization is 0.4.

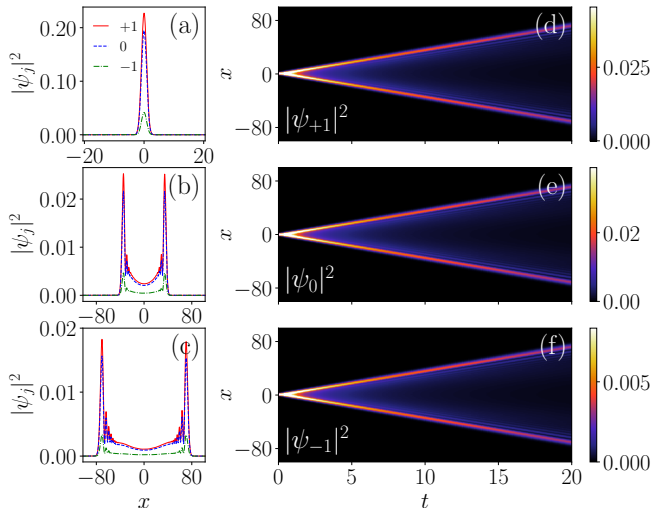


FIG. 8. Plots displaying the real-time expansion of a Bose-Einstein condensate (BEC) with coupling parameters $\Omega = 2$ and $k_L = 5$, as computed numerically with nonlinearities $c_0 = 0.25$ and $c_2 = -0.001$, and magnetization of 0.4 at different times: (a) $t = 0$, (b) $t = 25$, and (c) $t = 50$. The space-time plot shows the dynamics of the densities for (d) $|\psi_{+1}|^2$, (e) $|\psi_0|^2$, and (f) $|\psi_{-1}|^2$.

We have also observed a SIP for attractive interactions in Fig. 9, which shows the numerically calculated real-time propagation of the three component densities ψ_j where $j = 0, \pm 1$ of a quasi-1D ferromagnetic BEC with the release of the harmonic trap, with nonlinearities being $c_0 = -1.5$ and $c_2 = -0.3$. Figs. 9(a), 9(b), and 9(c) show the expansion dynamics when the magnetization is zero, which emphasizes that the density expansion is the same for ψ_{+1} and ψ_{-1} , whereas it is different for ψ_0 . On the other hand, Figs. 9(d), 9(e), and 9(f) correspond to the expansion dynamics when the magnetization is 0.4, demonstrating that the density expansion is different for all three cases, which indicates the removal of degeneracy. Moreover, one can also observe a clear expansion of the self-interference packet with time evolution.

B. Velocity profile during expansion and phase transition

Next, we shall investigate the velocity profile of the condensate during symmetric expansion. We calculate the expansion velocity during time evolution by recording the time taken for the expanding wavefront, with a threshold amplitude typically a few percent of the maximum amplitude, to cross each spatial grid point. Fig. 10 depicts the distance versus time graph of the expanding condensate for various values of Ω , with k_L fixed at 5 and without magnetization. The plot drives home the point that for small values of Rabi frequency, i.e., when $\Omega = 1$ and $\Omega = 2$, the wave packet expands faster in a shorter

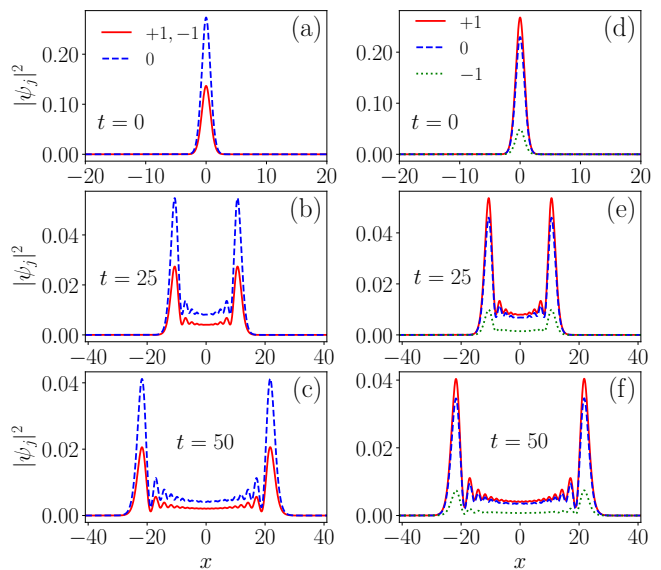


FIG. 9. Plots illustrating the evolution of spin-component densities, $|\psi_j|^2$, for coupling parameters $\Omega = 2$ and $k_L = 5$ and interaction strengths of $c_0 = -1.5$ and $c_2 = -0.3$ at different instances of time: (a)-(c) depict the scenario where magnetization is absent, while (d)-(f) corresponds to the case where magnetization is present. The time instances shown are $t = 0$, $t = 25$, and $t = 50$.

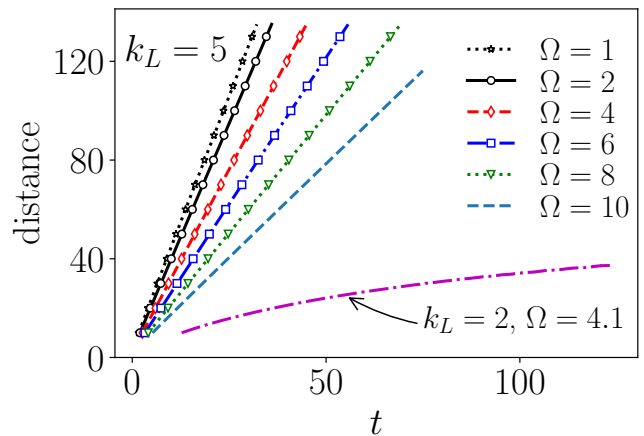


FIG. 10. Distance versus time plot showing the expansion for various values of Ω , with k_L fixed at 5 (without magnetization). The slopes of these curves correspond to the expansion velocities and are $v = 4.10$ ($\Omega = 1$), 3.64 ($\Omega = 2$), 2.94 ($\Omega = 4$), 2.38 ($\Omega = 6$), 1.92 ($\Omega = 8$) and 1.52 ($\Omega = 10$) in units $l_0 \times \omega_x$. The magenta dash-dotted line corresponds to $k_L = 2$ and $\Omega = 4.1$ showing the self-trapping of BECs

interval of time. The wave packet expansion slows down as we increase the Rabi coupling, as seen in the cases of both $\Omega = 3$ and $\Omega = 4$. When $\Omega = 6, 8$, or 10 , the expansion of the condensate slows down significantly and could eventually halt altogether. This phenomenon is referred to as “self-trapping” and is a potential signature of a negative mass regime. The velocity profile exhib-

ited during the condensate expansion is comparable to the one observed in a prior study, namely Ref. [16].

Fig. 11 shows the dynamics of self-trapped Bose-Einstein condensates for coupling parameters, for example, $\Omega = 4.1$ and $k_L = 2$ at different intervals of times. It is observed from the time evolution plot that self-

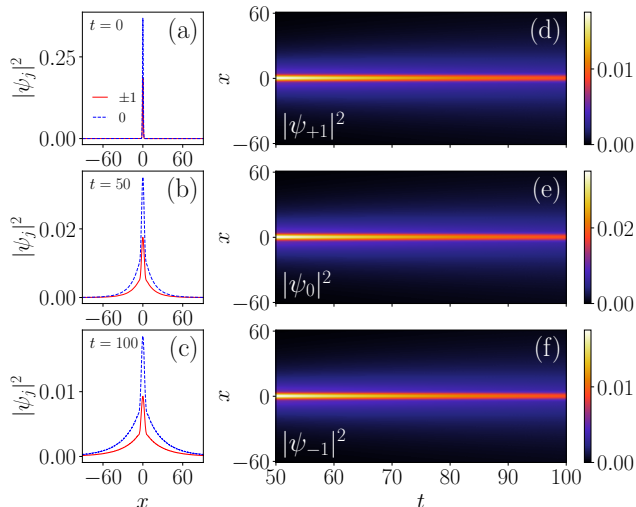


FIG. 11. Plots illustrating the dynamics of self-trapped Bose-Einstein condensates (BEC) with coupling parameters $\Omega = 4.1$ and $k_L = 2$, computed numerically with nonlinearities $c_0 = 0.25$ and $c_2 = -0.001$, without magnetization at different times: (a) $t = 0$, (b) $t = 50$, and (c) $t = 100$. The space-time plot shows the evolution of the density profiles for (d) $|\psi_{+1}|^2$, (e) $|\psi_0|^2$, and (f) $|\psi_{-1}|^2$.

trapping can occur due to the nonlinearity of the interactions between the atoms, which results in the formation of a localized region of high density known as a soliton. In this case, the atoms themselves create a potential well when the interactions are strong. The self-trapping phenomenon in BECs has many applications, such as matter-wave interferometry, atom optics, and quantum information processing [39]. It is worth pointing out at this juncture that the introduction of magnetization does not impact the dynamics of self-trapped BECs as well.

We study the expansion velocity of the condensate for different combinations of k_L and Ω . Figs. 12(a) and 12(b) show the variation of expansion velocity as a function of k_L for different values of Ω for attractive and repulsive interactions, respectively. It may be observed that the velocity decreases for small values of k_L and reaches a minimum close to zero at a critical value. After this critical k_L , the velocity increases linearly with k_L which is shown in Fig. 12(a). Similarly, in Fig. 12(b) for small values of k_L , the velocity is nearly equal to zero and there is a sudden increase in velocity after the critical point. Another interesting observation is that the critical value of k_L that separates the condensates with different velocity profiles is almost the same except that for attractive interactions, the momentum is imparted to the condensates only after the critical value. This implies that the

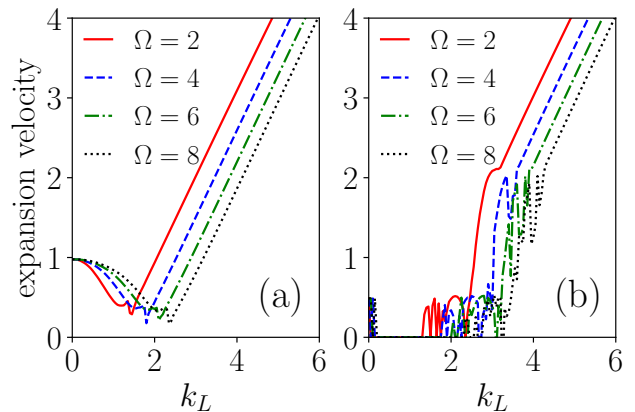


FIG. 12. The plot of the wave-packet expansion velocity as a function of k_L for different values of Ω , with (a) $c_0 = 0.25$ and $c_2 = -0.001$ (repulsive interaction) and (b) $c_0 = -1.5$ and $c_2 = -0.3$ (attractive interaction), in the absence of magnetization.

self trapping of the condensates is more pronounced in attractive interactions.

In addition, we have numerically computed the expansion velocities in the $k_L - \Omega$ plane for a range of values: $k_L \in [0, 6]$ and $\Omega \in [0, 8]$. Fig. 13(a) illustrates a phase diagram of the velocity profiles of the expanding wave-packet front in the $k_L - \Omega$ plane for the repulsive case with $c_0 = 0.25$ and $c_2 = -0.001$. Based on these figures, we observe that the velocity patterns are non-uniform and vary according to the values of k_L and Ω . By varying k_L and Ω , we have observed that the expansion velocity approaches zero for certain critical values of these parameters. At the critical point, there is an effective localization. This observation suggests the occurrence of a quantum phase transition, which is actually from the plane wave to the stripe wave phase. To determine the critical values of k_L and Ω , we examined the density profiles of the condensate. The values we obtained are consistent with those computed using the single-particle dispersion relation described in Eq. (5). The dispersion relation predicts a plane wave (PW) phase for $\Omega < k_L^2$ and a stripe wave (SW) phase for $\Omega > k_L^2$.

Similarly, in Fig. 13(b), we show the velocity profiles of the expanding wave-packet front as a function of the strengths of the SO and Rabi couplings, k_L and Ω , for the attractive case with $c_0 = -1.5$ and $c_2 = -0.3$. We can see that the velocity is equal to zero, and the condensate does not expand for small values of the SO coupling strength. However, for large k_L , the velocity patterns resemble those of the repulsive case shown in Fig. 13(a). Since the system is attractive, it is quite natural to observe self-trapping for small values of k_L . The phase transition from the plane wave phase to the stripe phase occurs close to the analytical prediction, which is $\Omega = k_L^2$. Similar phase transitions have been reported for harmonic traps in previous works [40–42].

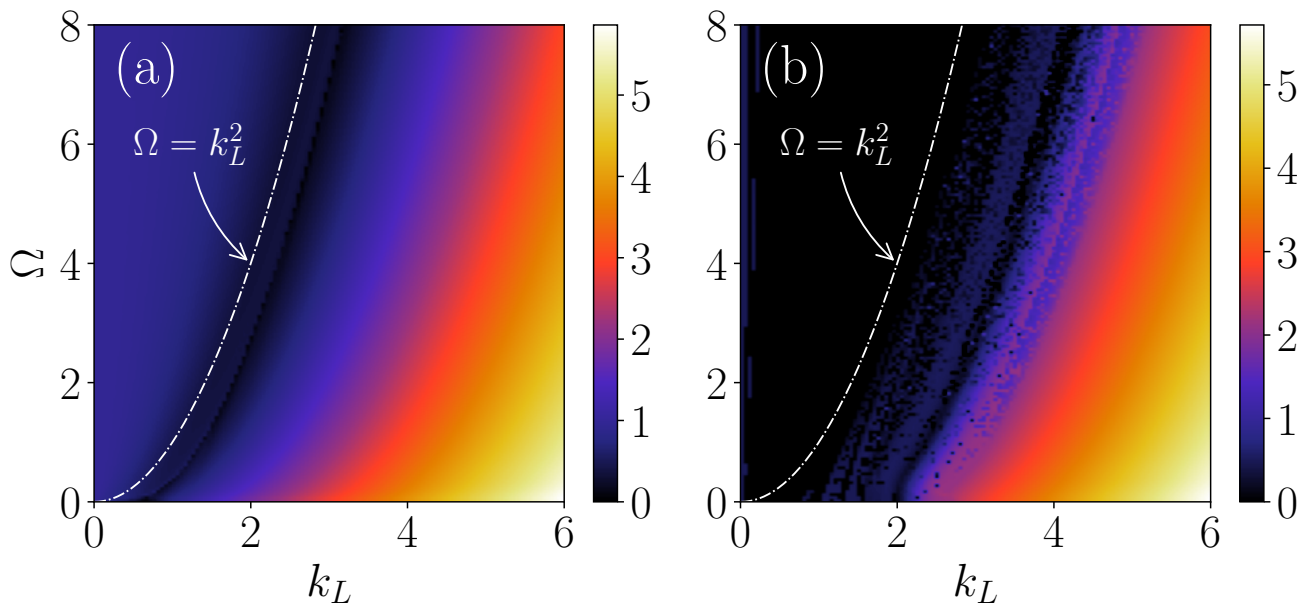


FIG. 13. Phase diagram illustrating the wave-packet expansion velocity as a function of k_L and Ω , with (a) $c_0 = 0.25$ and $c_2 = -0.001$ (repulsive interaction) and (b) $c_0 = -1.5$ and $c_2 = -0.3$ (attractive interaction), in the absence of magnetization. The theoretical $\Omega = k_L^2$ boundary, where the transition from plane wave to stripe pattern occurs, is denoted by the white-dash-dotted curve.

V. CONCLUSION

In this paper, we have investigated the dynamics of $F = 1$ spinor spin-orbit coupled BECs described by a three coupled GP equation in a range where the effective mass becomes negative due to the interplay between SO coupling and Rabi coupling. The density and time evolution profiles of the condensates show the existence of self-interfering packets (SIPs) for different coupling parameters for magnetized and unmagnetized states for both repulsive and attractive interactions. The density fluctuations are observed from the center to the tail, and we have found that increasing Ω while keeping k_L constant reduces the expansion. Our investigation highlights the observation of a symmetric double-well potential that identifies two stable regimes, in contrast, to spin-1/2 SOC BECs. Our results suggest the possibility of observing multiple stable states based on the SO coupling, Rabi coupling, and interaction strength. Furthermore, we have

observed a quantum phase transition from a plane wave phase to a stripe wave phase, where the expansion velocity becomes nearly zero. This transition may have wider ramifications in the areas of quantum and condensed matter physics. Besides, several signatures associated with the negative mass regime, such as symmetric expansion, pile-up, modulation instability, slowdown, and self-trapping, have also been identified, in addition to SIP.

ACKNOWLEDGMENTS

KR acknowledges financial support from UGC-SJSGC. SB and RR wish to thank the Council of Scientific and Industrial Research (CSIR), the Government of India for the financial support under Grant No. 03(1456)/19/EMR-II. The work of P.M. is supported by DST-SERB under Grant No. CRG/2019/004059, FIST (Department of Physics), and MoE RUSA 2.0 (Physical Sciences) Programmes.

-
- [1] G. Juzeliūnas, J. Ruseckas, P. Öhberg, and M. Fleischhauer, Light-induced effective magnetic fields for ultracold atoms in planar geometries, *Phys. Rev. A* **73**, 025602 (2006).
 - [2] Y.-J. Lin, R. Compton, A. Perry, W. Phillips, J. Porto, and I. Spielman, Bose-Einstein condensate in a uniform light-induced vector potential, *Phys. Rev. Lett.* **102**, 130401 (2009).
 - [3] M. Z. Hasan and C. L. Kane, Colloquium: Topological insulators, *Rev. Mod. Phys.* **82**, 3045 (2010).
 - [4] X.-L. Qi and S.-C. Zhang, Topological insulators and superconductors, *Rev. Mod. Phys.* **83**, 1057 (2011).
 - [5] K. von Klitzing, The quantized Hall effect, *Rev. Mod. Phys.* **58**, 519 (1986).
 - [6] F. Wilczek, Majorana returns, *Nat. Phys.* **5**, 614 (2009).
 - [7] J. D. Koralek, C. P. Weber, J. Orenstein, B. A. Bernevig, S.-C. Zhang, S. Mack, and D. D. Awschalom, Emergence of the persistent spin helix in semiconductor quantum wells, *Nature* **458**, 610 (2009).

- [8] J. Alicea, Y. Oreg, G. Refael, F. von Oppen, and M. P. A. Fisher, Non-abelian statistics and topological quantum information processing in 1d wire networks, *Nat. Phys.* **7**, 412 (2011).
- [9] Y.-J. Lin, R. L. Compton, K. Jiménez-García, J. V. Porto, and I. B. Spielman, Synthetic magnetic fields for ultracold neutral atoms, *Nature* **462**, 628 (2009).
- [10] B. Paredes, A. Widera, V. Murg, O. Mandel, S. Fölling, I. Cirac, G. V. Shlyapnikov, T. W. Hänsch, and I. Bloch, Tonks-Girardeau gas of ultracold atoms in an optical lattice, *Nature* **429**, 277 (2004).
- [11] T. Kinoshita, T. Wenger, and D. S. Weiss, Observation of a one-dimensional Tonks-Girardeau gas, *Science* **305**, 1125 (2004).
- [12] Z. Hadzibabic, P. Krüger, M. Cheneau, B. Battelier, and J. Dalibard, Berezinskii-Kosterlitz-Thouless crossover in a trapped atomic gas, *Nature* **441**, 1118 (2006).
- [13] Y.-J. Lin, K. Jiménez-García, and I. B. Spielman, Spin-orbit-coupled Bose-Einstein condensates, *Nature* **471**, 83 (2011).
- [14] M. Gong, S. Tewari, and C. Zhang, BCS-BEC crossover and topological phase transition in 3d spin-orbit coupled degenerate Fermi gases, *Phys. Rev. Lett.* **107**, 195303 (2011).
- [15] B. Eiermann, P. Treutlein, T. Anker, M. Albiez, M. Taglieber, K.-P. Marzlin, and M. K. Oberthaler, Dispersion management for atomic matter waves, *Phys. Rev. Lett.* **91**, 060402 (2003).
- [16] M. A. Khomechi, K. Hossain, M. E. Mossman, Y. Zhang, T. Busch, M. M. Forbes, and P. Engels, Negative-mass hydrodynamics in a spin-orbit-coupled Bose-Einstein condensate, *Phys. Rev. Lett.* **118**, 155301 (2017).
- [17] L.-C. Zhao, W. Wang, Q. Tang, Z.-Y. Yang, W.-L. Yang, and J. Liu, Spin soliton with a negative-positive mass transition, *Phys. Rev. A* **101**, 043621 (2020).
- [18] A. Farolfi, D. Trypogeorgos, C. Mordini, G. Lamporesi, , and G. Ferrari, Observation of magnetic solitons in two-component Bose-Einstein condensates, *Phys. Rev. Lett.* **125**, 030401 (2020).
- [19] X. Chai, D. Lao, K. Fujimoto, R. Hamazaki, M. Ueda, and C. Raman, Magnetic solitons in a spin-1 Bose-Einstein condensate, *Phys. Rev. Lett.* **125**, 030402 (2020).
- [20] L.-Z. Meng, S.-W. Guan, and L.-C. Zhao, Negative mass effects of a spin soliton in Bose-Einstein condensates, *Phys. Rev. A* **105**, 013303 (2022).
- [21] D. Colas, F. P. Laussy, and M. J. Davis, Negative-mass effects in spin-orbit coupled Bose-Einstein condensates, *Phys. Rev. Lett.* **121**, 055302 (2018).
- [22] C. J. Pethick and H. Smith, *Bose-Einstein Condensation in Dilute Gases*, 2nd ed. (Cambridge University Press, 2008).
- [23] S. Gautam and S. K. Adhikari, Phase separation in a spin-orbit-coupled Bose-Einstein condensate, *Phys. Rev. A* **90**, 043619 (2014).
- [24] T.-L. Ho, Spinor Bose condensates in optical traps, *Phys. Rev. Lett.* **81**, 742 (1998).
- [25] L. Salasnich, A. Parola, and L. Reatto, Effective wave equations for the dynamics of cigar-shaped and disk-shaped Bose condensates, *Phys. Rev. A* **65**, 043614 (2002).
- [26] Y. Kawaguchi and M. Ueda, Spinor Bose-Einstein condensates, *Phys. Rep.* **520**, 253 (2012).
- [27] S. Gautam and S. K. Adhikari, Spontaneous symmetry breaking in a spin-orbit-coupled $f = 2$ spinor condensate, *Phys. Rev. A* **91**, 013624 (2015).
- [28] R. Ravisankar, D. Vudragović, P. Muruganandam, A. Balaž, and S. K. Adhikari, Spin-1 spin-orbit- and Rabi-coupled Bose-Einstein condensate solver, *Comput. Phys. Commun.* **259**, 107657 (2021).
- [29] T. Anker, M. Albiez, R. Gati, S. Hunsmann, B. Eiermann, A. Trombettoni, and M. K. Oberthaler, Nonlinear self-trapping of matter waves in periodic potentials, *Phys. Rev. Lett.* **94**, 020403 (2005).
- [30] P. Kaur, A. Roy, and S. Gautam, Fortress: Fortran programs for solving coupled gross-pitaevskii equations for spin-orbit coupled spin-1 Bose-Einstein condensate, *Comput. Phys. Commun.* **259**, 107671 (2021).
- [31] S. Inouye, M. R. Andrews, J. Stenger, H.-J. Miesner, D. M. Stamper-Kurn, and W. Ketterle, Observation of Feshbach resonances in a Bose-Einstein condensate, *Nat.* **392**, 151–154 (1998).
- [32] A. Marte, T. Volz, J. Schuster, S. Dürr, G. Rempe, E. G. M. van Kempen, and B. J. Verhaar, Feshbach resonances in Rubidium 87: Precision measurement and analysis, *Phys. Rev. Lett.* **89**, 283202 (2002).
- [33] C. Chin, Feshbach resonances in ultracold gases, *Rev. Mod. Phys.* **82**, 1225 (2010).
- [34] P. Muruganandam and S. Adhikari, Fortran programs for the time-dependent Gross-Pitaevskii equation in a fully anisotropic trap, *Comput. Phys. Commun.* **180**, 1888 (2009).
- [35] P. Muruganandam, A. Balaž, and S. K. Adhikari, Openmp solver for rotating spin-1 spin-orbit- and Rabi-coupled Bose-Einstein condensates, *Comput. Phys. Commun.* **264**, 107926 (2021).
- [36] C. Qu, L. P. Pitaevskii, and S. Stringari, Spin-orbit-coupling induced localization in the expansion of an interacting Bose-Einstein condensate, *New J. Phys.* **19**, 085006 (2017).
- [37] J. Su, H. Lyu, and Y. Zhang, Self-interfering dynamics in Bose-Einstein condensates with engineered dispersions, *Phys. Lett. A* **443**, 128218 (2022).
- [38] B. Wang, P. Fu, J. Liu, and B. Wu, Self-trapping of Bose-Einstein condensates in optical lattices, *Phys. Rev. A* **74**, 063610 (2006).
- [39] A. R. Kolovsky, Bright solitons and self-trapping with a Bose-Einstein condensate of atoms in driven tilted optical lattices, *Phys. Rev. A* **82**, 011601 (2010).
- [40] Y. Zhang, G. Chen, and C. Zhang, Tunable spin-orbit coupling and Quantum Phase Transition in a trapped Bose-Einstein condensate, *Sci. Rep.* **3**, 1937 (2013).
- [41] R. Ravisankar, T. Sriraman, L. Salasnich, and P. Muruganandam, Quenching dynamics of the bright solitons and other localized states in spin-orbit coupled Bose-Einstein condensates, *J. Phys. B: At. Mol. Opt. Phys.* **53**, 195301 (2020).
- [42] J. Cabedo and A. Celi, Excited-state quantum phase transitions in spin-orbit-coupled Bose gases, *Phys. Rev. Res.* **3**, 043215 (2021).